Simultaneous Emission-transmission Tomography (SET)

Lars Gjesteby, Wenxiang Cong, Ge Wang*

***Abstract* — A recently demonstrated imaging method combines MRI principles with nuclear medicine techniques to reconstruct a distribution of a polarized γ-ray emitting radioisotope. The resultant images achieve better spatial resolution than standard nuclear imaging and higher sensitivity than MRI. In this paper, we propose to acquire this form of MRI-modulated nuclear data for simultaneous image reconstruction in terms of both emission and transmission parameters, suggesting the potential for simultaneous CT-MRI-SPECT. The complementary information provides insight into tissue forms and molecular/cellular functions of features being imaged. Numerical simulation results of a lung phantom support the mathematical basis of our "SET" technique. Additional considerations are presented regarding the radiotracer characteristics and the imaging hardware.**

***Keywords* — Magnetic resonance imaging (MRI), single photon emission computed tomography (SPECT), polarized radiotracers, computed tomography (CT), multimodality imaging**

I. INTRODUCTION

The medical imaging field has been greatly advanced by research and development of multimodality imaging systems and methods, such as hybrid modalities that combine positron emission tomography (PET) with CT and MRI respectively. Simultaneous PET-CT provides functional data that is co-registered with structural information from CT in a single image [1]. PET-MRI delivers complementary functional and morphological information by providing the rich soft tissue contrast of MRI to the tomographic map of high-sensitivity radiotracers from PET [2]. The synergy of nuclear medicine with high resolution tomographic techniques has led to breakthroughs in diagnostics and therapy [3], [4].

A novel imaging method that integrates MRI principles with nuclear medicine techniques was recently demonstrated by Zheng *et al.* [5]. Their method, referred to as polarized nuclear imaging (PNI), produces pilot images that display the distribution of a polarized radioactive tracer with better localization than standard nuclear imaging and higher sensitivity than MRI. Here we propose to improve upon this technique by reconstructing not only the concentration image, but also the attenuation image. We refer to our approach as simultaneous emission-transmission tomography (SET), with which both emission and transmission images can be reconstructed through measurement and analysis of γ-ray data.

The main goal of this paper is to present the SET imaging principles. First, we describe the methodology involving the system design with emphasis on the imaging protocol and the formulation for image inversion. As a prerequisite, we review aspects of the radioisotope as related to SET imaging purposes. Then, we present initial numerical results to demonstrate the feasibility of SET for reconstructing concentration and attenuation images of a water phantom with various radio-labeled tissue types. Finally, we discuss next steps toward a physical prototype for SET and beyond.

II. METHODOLOGY

A. Imaging system

For our proposed SET imaging process, polarized radioactive tracers are injected into an animal or patient being imaged. Polarization of the radiotracer can be achieved by the spin-exchange optical pumping technique, which uses infrared laser light to rearrange electrons [6]. A main background magnetic field B_0 aligns the polarized radiotracer molecules along the axis of the main field (the z-direction). This field can be created by Helmholtz coils (strength may be less than 0.1 T). One pair of γ-ray detectors is situated along the x-direction and one pair along the y-direction. The collimator grids coupled to the detectors allow only directionally specified incident γ-rays to be measured.

Gradient coils will first alter the B_0 field along the x-direction with a B_1 gradient field. The RF coil will apply a pulse at the Larmor frequency to flip the polarized radiotracers to align in the transverse direction. Only radiotracers in a selected section of the B_1 field will be affected to undergo precession at the targeted Larmor frequency. Now, emitted γ-rays can be detected by the longitudinal detectors along the manipulated lines perpendicular to the selected section, and the detected γ-rays can only be from the target region. This process can be repeated at each of multiple Larmor frequencies to detect signals from all sections. To image in a second dimension, gradient coils can then alter the B_0 field along the y-direction.

Our exemplary system design, shown in Fig. 1, consists of two pairs of γ-ray detectors with collimators, Helmholtz coils to produce the main magnetic field, gradient coils to alter the field strength in the x- and y-directions, RF coils, and an object stage. Other design possibilities exist, such as a rotating gantry to spin a pair of collimated detector arrays.

DOI: 10.12059/Fully3D.2017-11-3104003

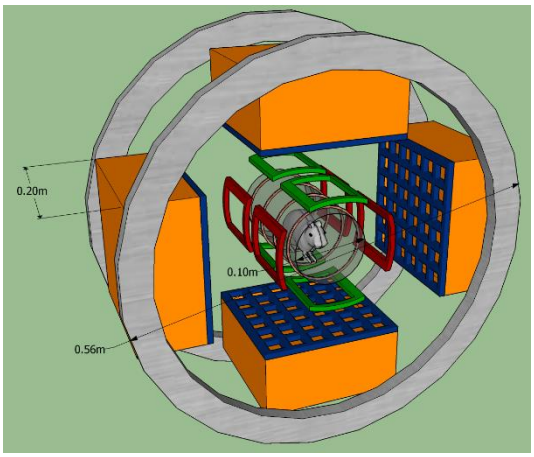

Fig. 1. System design for SET containing Helmholtz coils (gray – 0.56 m in diameter and spaced 0.2 m apart), gradient coils (red and green), RF coils (transparent cylinder – 0.1 m in diameter and 0.2 m long), and γ-ray detectors with collimators (orange and blue – 0.2 m by 0.2 m).

B. Radiotracers

Zheng *et al.* employed hyperpolarized ^{131m}Xe as the radiotracer in the PNI feasibility study. This isotope was suitable for their proof of concept demonstration, but it presents challenges for clinical use. The half-life is 12 days and multiple cycles of polarization were needed to complete the data acquisition process. There are a few primary characteristics that an ideal radiotracer for SET should have. First, the material must be compatible with the spin-exchange optical pumping technique so that a majority portion (at least 60%) of the nuclei can be polarized. The nuclei spin number must be greater than ½ to achieve anisotropic γ-ray emission. Third, a more realistic half-life for the radiotracer would be on the scale of minutes to hours, instead of days, to enable faster image acquisition. Lastly, the isotope should have a favorable γ-ray branching ratio (at least 20%).

An alternate isotope of xenon, ^{127m}Xe, exhibits a much shorter half-life at 69 seconds while maintaining the biocompatibility similar to ^{131m}Xe. The branching ratio is at 38%, as compared to 2% for ^{131m}Xe, which provides a substantial increase in the amount of γ decays that can be used for imaging. Another candidate is ^{79m}Kr, which has a half-life of 50 seconds and a branching ratio of 27%. Previous studies have employed ^{127m}Xe and ^{79m}Kr isotopes for clinical nuclear imaging [7], [8]. Table 1 summarizes characteristics of the three radiotracers discussed here, which can be detected using conventional detectors, or even potentially novel ones [9] (see Discussion for more).

TABLE 1. Characteristics of candidate radioisotopes for SET

Isotope	Half-life	γ-ray Emission Energy (keV)	γ-ray Branching Ratio
^{131m}Xe	12 days	164	2%
^{127m}Xe	69 sec	124.8-172.5	38%
^{79m}Kr	50 sec	130	27%

C. Mathematical basis

The innovation of our method is to reconstruct both the radiotracer concentration and the background attenuation simultaneously. Detectors on the top, bottom, and both sides of the object detect γ-rays, but the attenuation background through which the γ-rays travel will be different. The γ-rays emitted from radioactive tracers at position r can be measured by a pair of detectors as follows:

$$m_1(r) = \Phi(r)\, exp\left(-\int_{-\infty}^{r} \mu(r)dr\right)$$
$$m_2(r) = \Phi(r)\, exp\left(-\int_{r}^{\infty} \mu(r)dr\right) \quad (1)$$

where $\Phi(r)$ is the γ-rays intensity at position r which is related to the concentration $\lambda(r)$ of a radioactive tracer, $\mu(r)$ is the attenuation coefficient of γ-rays at position r, and m_1 and m_2 are paired data. Our purpose is to reconstruct images of both the attenuation $\mu(r)$ and the concentration $\lambda(r)$ simultaneously. When there is a sufficient concentration of radioactive tracers at position r so that the radioactive tracer emits a sufficiently high flux of γ-rays ($\Phi(r)>0$), an integral equation with respect to the attenuation coefficient of the object can be obtained from Eq. (1):

$$\log\left(\frac{m_1(r)}{m_2(r)}\right) = \int_{r}^{\infty} \mu(r)dr - \int_{-\infty}^{r} \mu(r)dr \quad (2)$$

Eq. (2) is a linear integral equation, which permits an inverse solution to recover the attenuation coefficient image of γ-rays. Eq. (2) can be discretized into a linear equation with respect to the attenuation coefficient $\mu(r)$ from the measured data for each γ-ray detector element at every position r. Thus, a system of linear equations can be established from all γ-ray detectors:

$$Ax = b \quad (3)$$

where $\boldsymbol{A}$ is a system matrix, x is a vector discretizing unknown attenuation coefficients, and b is a vector that is computed from measurement data according to Eq. (2). The reconstruction method for attenuation coefficients requires a sufficiently large support of the underlying radioactive tracer distribution, which is certainly reasonable (no tracer, no data). Recently developed compressed sensing (CS) techniques can offer high-quality image reconstruction from fewer incoherent measurements than what is required by the Shannon-Nyquist sampling theorem. Based on Eq. (3), a CS-based iterative algorithm can be used to perform the attenuation image reconstruction for noise suppression and contrast improvement. Furthermore, the concentration $\lambda(r)$ of the radioactive tracer, related to intensity $\Phi(r)$, can be reconstructed from Eq. (1) and the reconstructed attenuation factor from γ-ray measurements:

$$\Phi(r) = exp\left(\int_{-\infty}^{r} \mu(r)dr\right) m_1(r)$$
$$\Phi(r) = exp\left(\int_{r}^{\infty} \mu(r)dr\right) m_2(r) \quad (4)$$

The above derivation is in the continuous domain. For numerical implementation, an accurate discretization scheme is needed. Care should be taken when γ-rays are simultaneously emitted and attenuated by a uniform pixel/voxel. A discrete model can be formulated for such a pixel/voxel of width a as shown in Fig. 2.

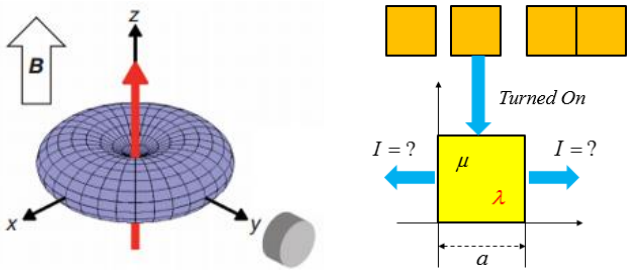

(a) (b)

Fig. 2. For a given detector element (gray), (a) any pixel/voxel can be magnetically turned on or off (adapted from [5]), and (b) γ-rays are simultaneously emitted and attenuated by this pixel/voxel.

Then, the intensity measurement on an active side of the pixel/voxel can be expressed as follows:

$$\begin{aligned} I &= \int_0^a \lambda\, exp(-\mu(a-r))dr \\ &= \lambda\, exp(-\mu a)\int_0^a exp(\mu r)\, dr \\ &= \frac{\lambda\, exp(-\mu a)}{\mu}\int_0^a exp(\mu r)\, d\mu r \\ &= \frac{\lambda\, exp(-\mu a)}{\mu}(exp(\mu a)-1) \end{aligned} \tag{5}$$

Equivalently, the discrete model for any pixel/voxel in the ith row and jth column is as follows:

$$I_{ij} = \frac{\lambda_{ij} exp(-\mu_{ij} a)}{\mu_{ij}}\left(exp(\mu_{ij} a)-1\right) \tag{6}$$

With I_{ij} from the active pixel/voxel, the further propagation/attenuation process towards a detector element can be simply modeled according to a discretized Beer–Lambert law. In this way, the system matrix $\boldsymbol{A}$ can be constructed. Finally, a discretized counterpart of Eq. (4) can be similarly obtained (solving Eq. (6) for λ_{ij} from known attenuation coefficients and I_{ij}). Pseudocode describing the reconstruction process is listed as follows:

Reconstruct the attenuation coefficients

- Do the following for each pixel (row, column) if measured intensity is non-zero:
  - Set the component of b corresponding to active pixel to the logarithmic ratio of measurements from detectors 1 and 2 (Eq. 2)
  - Construct the corresponding rows and columns of system matrix A. The coefficients contained in A depend on pixel positions relative to the active pixel
- Solve the inverse problem to recover attenuation coefficients

Recover the radiotracer concentration distribution

- Do the following for each pixel along the row direction:
  - Find flux escaping each side of the pixel using the Beer-Lambert law in reverse order in terms of the reconstructed attenuation coefficients and known intensity measurements from each detector
  - Compute the average of the two flux estimates
  - Solve for the concentration of the pixel using Eq. 6

D. Whole-body SPECT-CT Concept

Whole-body PET is a promising research tool currently under development at University of California, Davis [10], [11]. By extending the field of view over the entire length of the body, nearly all photons emitted can be captured by a cylindrical detector surface. The idea behind this effort could be adapted for our SET approach to perform whole-body SPECT-CT in an MRI framework. This technology would allow a significant increase in image sensitivity orders of magnitude higher than conventional nuclear imaging methods [11]. Fig. 3 illustrates an example system design.

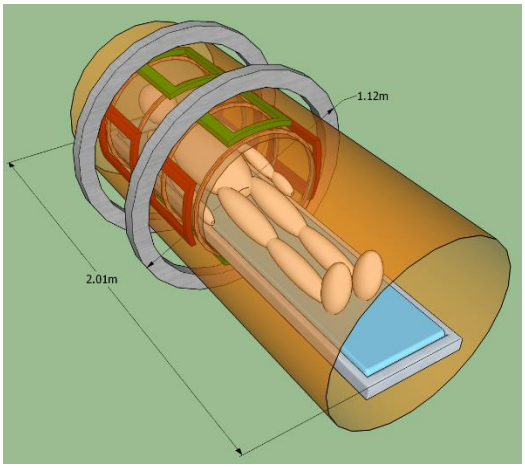

Fig. 3. System design for whole-body SPECT-CT containing Helmholtz coils (gray), gradient coils (red and green), a cylindrical γ-ray detector array (orange), and a patient table. Note that for clarity only a top portion of MR components are shown for the whole-body SPECT-CT system rendering.

III. NUMERICAL SIMULATION

A lung phantom from the visible human project [12] was adapted to demonstrate SET numerically using Eqs. (1-6). We assumed that a radiotracer was distributed in the whole phantom with a background concentration of 0.05 MBq/ml, and that it became more concentrated in regions of interest (ROIs) [13], [14]. Specifically, eight ROIs were defined with concentrations ranging from 0.150 to 0.325 MBq/ml. Then, the γ-ray intensity measurements were simulated based on our discretized forward model. For simplicity, the simulation is not tailored to a specific radionuclide or decay time. The pixel size was set to 0.5 mm and the image matrix was made 128 x 128. From the m_1 and m_2 measurements, the attenuation and concentration images were reconstructed.

Fig. 4 displays the ground truth and the reconstructed images of the attenuation values, as well as the corresponding difference image. In the noise-free case, the least squares residual was approximately 0.001, and the largest errors in attenuation coefficient occurred across the boundaries of the lung and tissue regions. Next, the concentration images were calculated from the estimated attenuation values. Fig. 5 shows the ground truth and reconstructed images of the radiotracer distribution, along with the difference image. Error propagation is evident from the estimated attenuation values, as the mean concentration errors in the ROIs are between 2.1% and 3.2%, as noted in Fig. 5c.

To simulate noisy measurements, the Poisson distribution was assumed with the ideal measurement value set as the mean of the random variable. The acquisition interval was increased up to 1000 a.u. to increase photon counts in detector cells. Fig. 6 shows the attenuation and radiotracer concentration images reconstructed from simulated noisy data, along with the respective difference images. The reconstruction steps are the same as those used to produce Figs. 4 and 5, except that data were produced with Poisson noise incorporated. The MATLAB code used for simulations is contained in the Appendix.

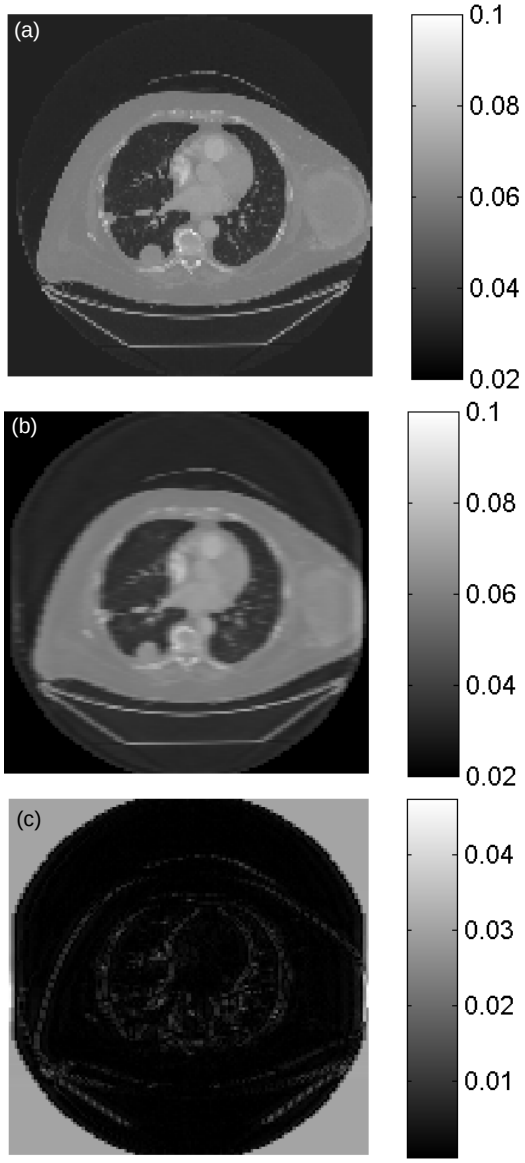

Fig. 4. Attenuation images (cm^{-1}) obtained from the numerical phantom. (a) The ground truth, (b) the reconstruction result, and (c) the difference image.

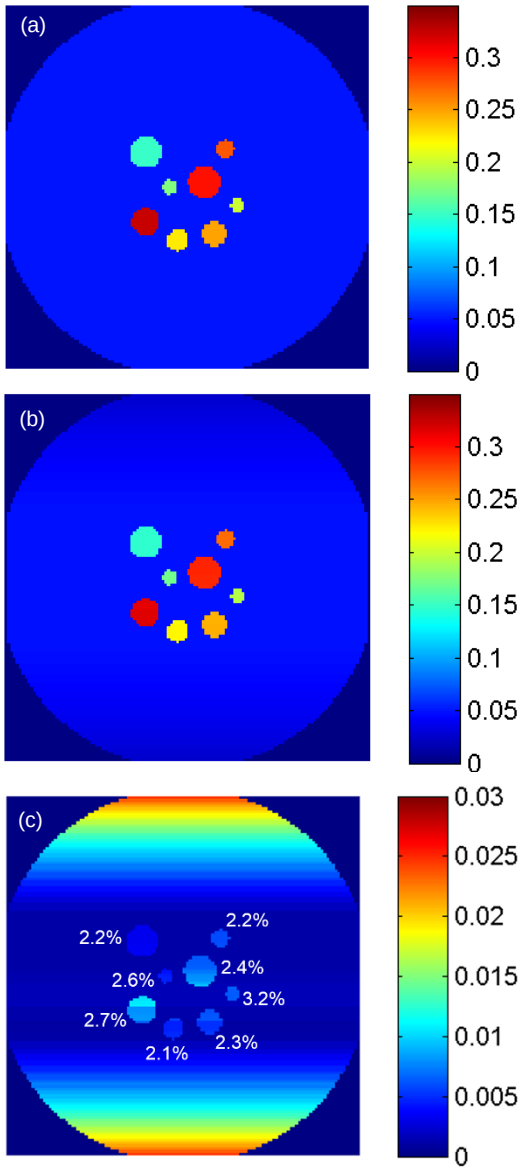

Fig. 5. Radiotracer concentration images (MBq/ml) obtained from the numerical phantom. (a) The ground truth, (b) the reconstruction result, and (c) the difference image with mean error percentages for each ROI shown in white.

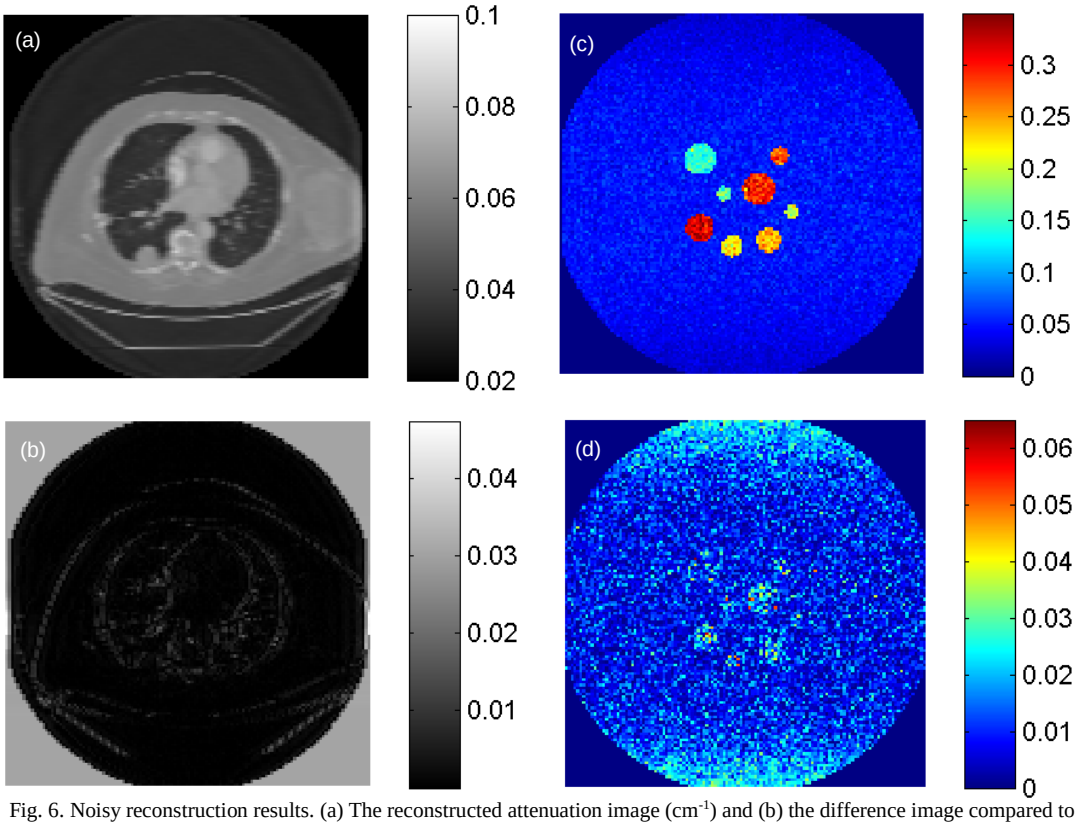

Fig. 6. Noisy reconstruction results. (a) The reconstructed attenuation image (cm^{-1}) and (b) the difference image compared to the ground truth (Fig. 4a), as well as (c) the reconstructed radiotracer concentration image (MBq/ml) and (d) the difference image compared to the ground truth (Fig. 5a).

IV. DISCUSSION AND CONCLUSION

Improving on the work by Zheng *et al.*, this paper presents the initiative and formulation for SET–simultaneous emission-transmission tomography–and demonstrates initial results obtained from numerical simulation. Our reconstruction scheme shows that, in principle, the radiotracer concentration can be determined with high accuracy. For attenuation estimation, our results indicate that the boundaries of tissue regions are prone to the largest errors. Additionally, an iterative reconstruction method will suppress noise and artifacts in a reconstructed image. To perform a more realistic assessment of the imaging performance and improve the reconstruction scheme, physical experiments are needed on a prototype SET system.

While the energy spectra of γ-rays and x-rays overlap each other substantially, the current attenuation-based imaging tasks are typically performed with x-rays with an external radiation source, the x-ray tube. In our proposed SET scheme, radiotracers are used to serve as internal sources for attenuation-based imaging. One of the merits is that the attenuation paths from such an internal source distribution to the detectors will be greatly reduced, thereby improving the signal-to-noise ratio and reducing the requisite radiation dose. This enables a new opportunity for low-dose CT, as for a given image quality, fewer photons would be needed compared to conventional CT methods. Also, the SET system is quite similar to the MRI system, and can be equipped for MRI as well. By doing so, we see several trinity system possibilities capable of CT-MRI-SPECT, which represents a higher level synergy relative to dual-modality scanners such as PET-CT, PET-MRI, and CT-MRI under discussion in other papers.

There are several possibilities for constructing the magnet subsystem of a SET prototype. A conventional Helmholtz coil with a field strength of less than 0.1 T would be the most straightforward. An alternative is to employ an emerging technology, superconducting fibers, to create the magnetic field more efficiently [15]. After injection with liquid helium, the fibers are capable of exhibiting superconductivity for an extended period of time [16]. These may be wound into coils to achieve a homogeneous local magnetic field with less power consumption. Further analysis is also needed on radioisotope candidates to determine which ones are most feasible for SET. The ideal material would have a half-life on the order of minutes to hours and a longitudinal relaxation on the order of tens of seconds, and be capable of being polarized by spin-exchange optical pumping.

Polarization of scattered x-rays or γ-rays is linked to the directionally-dependent scatter probability as defined by the Klein-Nishina differential cross-section [17]. The polarization information of photons can be detected as an alternate means to identify coincidences and form images in PET. This method was shown to significantly improve coincidence detection

accuracy, even at high emission rates [9]. Polarization detection gives rise to "electromagnetic collimation," in which photons are sorted by their inherent wave properties upon detection to determine their origins. This could be utilized for SET, and will be explored in our future work.

The novelty of SET is that it provides simultaneous emission and transmission data calculated from γ-ray measurements of a precise region of polarized radionuclide. The background attenuation metrics deliver morphological insight in addition to the functional information from radiotracer concentration. A physical system with this imaging capability would be broadly applicable to analyze many types of biomedical problems. Previous studies explored xenon isotopes for *in vivo* biosensors [18]–[20], and SET provides a novel imaging method to obtain higher sensitivity information from these materials in perfused regions of the body.

REFERENCES

[1] T. Beyer, D. W. Townsend, T. Brun, P. E. Kinahan, M. Charron, R. Roddy, J. Jerin, J. Young, L. Byars, and R. Nutt, "A combined PET/CT scanner for clinical oncology," *J Nucl Med*, vol. 41, pp. 1369–1379, 2000.

[2] M. S. Judenhofer, H. F. Wehrl, D. F. Newport, C. Catana, S. B. Siegel, M. Becker, A. Thielscher, M. Kneilling, M. P. Lichy, and M. Eichner, "Simultaneous PET-MRI: a new approach for functional and morphological imaging," *Nat. Med.*, vol. 14, no. 4, pp. 459–465, 2008.

[3] M. Charron, T. Beyer, N. N. Bohnen, P. E. Kinahan, M. Dachille, J. Jerin, R. Nutt, C. C. Meltzer, V. Villemagne, and D. W. Townsend, "Image analysis in patients with cancer studied with a combined PET and CT scanner," *Clin. Nucl. Med.*, vol. 25, no. 11, pp. 905–910, 2000.

[4] A. Boss, S. Bisdas, A. Kolb, M. Hofmann, U. Ernemann, C. D. Claussen, C. Pfannenberg, B. J. Pichler, M. Reimold, and L. Stegger, "Hybrid PET/MRI of intracranial masses: initial experiences and comparison to PET/CT," *J. Nucl. Med.*, vol. 51, no. 8, pp. 1198–1205, 2010.

[5] Y. Zheng, G. W. Miller, W. A. Tobias, and G. D. Cates, "A method for imaging and spectroscopy using γ-rays and magnetic resonance," *Nature*, vol. 537, no. 7622, pp. 652–655, 2016.

[6] T. G. Walker and W. Happer, "Spin-exchange optical pumping of noble-gas nuclei," *Rev. Mod. Phys.*, vol. 69, no. 2, p. 629, 1997.

[7] W. G. Myers, J. R. Dahl, and M. C. Graham, "Xenon-127m: a new radionuclide for applications in nuclear medicine.," *J. Nucl. Med. Off. Publ. Soc. Nucl. Med.*, vol. 31, no. 4, pp. 489–492, 1990.

[8] W. G. Myers, J. R. Dahl, and M. C. Graham, "Krypton-79m: a new radionuclide for applications in nuclear medicine.," *J. Nucl. Med. Off. Publ. Soc. Nucl. Med.*, vol. 27, no. 9, pp. 1436–1441, 1986.

[9] Z. Kuncic, A. McNamara, K. Wu, and D. Boardman, "Polarization enhanced X-ray imaging for biomedicine," *Nucl. Instruments Methods Phys. Res. Sect. A Accel. Spectrometers, Detect. Assoc. Equip.*, vol. 648, pp. S208–S210, 2011.

[10] S. R. Cherry, "The 2006 Henry N. Wagner Lecture: Of mice and men (and positrons)—advances in PET imaging technology," *J. Nucl. Med.*, vol. 47, no. 11, pp. 1735–1745, 2006.

[11] S. R. Cherry, R. D. Badawi, J. S. Karp, W. W. Moses, P. Price, and T. Jones, "Total-body imaging: Transforming the role of positron emission tomography.," *Sci. Transl. Med.*, vol. 9, no. 381, 2017.

[12] V. Spitzer, M. J. Ackerman, a. L. Scherzinger, and D. Whitlock, "The visible human male: a technical report.," *J. Am. Med. Inform. Assoc.*, vol. 3, no. 2, pp. 118–130, 1996.

[13] T. Kashiwagi, K. Yutani, M. Fukuchi, H. Naruse, T. Iwasaki, K. Yokozuka, S. Inoue, and S. Kondo, "Correction of nonuniform attenuation and image fusion in SPECT imaging by means of separate X-ray CT," *Ann. Nucl. Med.*, vol. 16, no. 4, pp. 255–261, 2002.

[14] S. J. McMahon, D. Young, Z. Ballok, B. S. Badaruddin, V. Larbpaiboonpong, and G. Hawdon, "Vascularity of the femoral head after Birmingham hip resurfacing. A technetium Tc 99m bone scan/single photon emission computed tomography study," *J. Arthroplasty*, vol. 21, no. 4, pp. 514–521, 2006.

[15] D. Homa, Y. Liang, G. Pickrell, D. Homa, Y. Liang, and G. Pickrell, "Superconducting fiber," *Appl. Phys. Lett.*, vol. 103, no. 82601, pp. 1–4, 2013.

[16] D. Homa, G. Kaur, G. Pickrell, and Y. Liang, "Efficient cooling of superconducting fiber core via holey cladding," *Cryogenics (Guildf).*, vol. 61, pp. 25–30, 2014.

[17] O. Klein and T. Nishina, "Über die Streuung von Strahlung durch freie Elektronen nach der neuen relativistischen Quantendynamik von Dirac," *Zeitschrift für Phys. A Hadron. Nucl.*, vol. 52, no. 11, pp. 853–868, 1929.

[18] S. D. Swanson, M. S. Rosen, K. P. Coulter, R. C. Welsh, and T. E. Chupp, "Distribution and dynamics of laser-polarized 129 Xe magnetization in vivo," *Magn. Reson. Med.*, vol. 42, no. 6, pp. 1137–1145, 1999.

[19] M. M. Spence, S. M. Rubin, I. E. Dimitrov, E. J. Ruiz, D. E. Wemmer, A. Pines, S. Q. Yao, F. Tian, and P. G. Schultz, "Functionalized xenon as a biosensor," *Proc. Natl. Acad. Sci.*, vol. 98, no. 19, pp. 10654–10657, 2001.

[20] H. M. Rose, C. Witte, F. Rossella, S. Klippel, C. Freund, and L. Schröder, "Development of an antibody-based, modular biosensor for 129Xe NMR molecular imaging of cells at nanomolar concentrations," *Proc. Natl. Acad. Sci.*, vol. 111, no. 32, pp. 11697–11702, 2014.

```
%%%%%%% Numerical Simulation for SET %%%%%%%%%%%
%%% Developed by Lars Gjesteby, Wenxiang Cong, and Ge Wang
clear all; clc;

N = 128;    % Number of pixels along each dimension
pixelsize = 0.5;   % Define pixel width in mm

%%%%% generate measurements of gamma rays
load('concentLung','concentrat'); load('attenLung','atten');

%% Synthesize data intensity measurements with two detectors
% Generate intensity at each pixel according to Eq. 6
I = zeros(N);I_poiss = zeros(N);
scalefactor = 1000; % Scale factor represents increased data acquisition time to handle
low counts for noise model
for ii=1:N
    for k=1:N
        I(ii,k) = (concentrat(ii,k)*(1-exp(-pixelsize*atten(ii,k)))/atten(ii,k));
        I_poiss(ii,k) = poissrnd(scalefactor*(concentrat(ii,k)*(1-exp(-pixelsize*atten
(ii,k)))/atten(ii,k)));
    end
end

m1 = zeros(N); m2 = zeros(N);
% Pure measurements at detectors by Beer-Lambert law
for ii =1:N
    m2(ii,1) = I(ii,1)*exp(-pixelsize*sum(atten(ii,2:N)));
    for k=2:N-1
        m1(ii,k) = I(ii,k)*exp(-pixelsize*sum(atten(ii,1:k-1)));
        m2(ii,k) = I(ii,k)*exp(-pixelsize*sum(atten(ii,k+1:N)));
    end
    m1(ii,N) = I(ii,N)*exp(-pixelsize*sum(atten(ii,1:N-1)));
end

% Poisson Noise added
m1_poiss = zeros(N); m2_poiss = zeros(N);
for ii =1:N
    m2_poiss(ii,1) = I_poiss(ii,1)*exp(-pixelsize*sum(atten(ii,2:N)));
    for k=2:N-1
        m1_poiss(ii,k) = I_poiss(ii,k)*exp(-pixelsize*sum(atten(ii,1:k-1)));
        m2_poiss(ii,k) = I_poiss(ii,k)*exp(-pixelsize*sum(atten(ii,k+1:N)));
    end
    m1_poiss(ii,N) = I_poiss(ii,N)*exp(-pixelsize*sum(atten(ii,1:N-1)));
end


%% Reconstruct attenuation coefficient images
% A is system matrix and b is the ratio of intensity measurements

%%%%%% Pure m1 and m2 measurements
col=0; A=zeros(1,N*N);
```

```
for ii =1:N
    row=N*(ii-1);
    col=col+1;
    % Special case for column 1
    if m1(ii,1)>eps & m2(ii,1)>eps          % check if measurement exists at each pixel
        b(col,1)=log(m1(ii,1)/m2(ii,1));
        A(col,row+1) = 0; A(col,(row+2):(row+N)) = -pixelsize;  % System matrix↙
coefficient is zero at the activated pixel and "-pixelsize" for all others
    end
    % General case for non-edge columns
    for k=2:N-1
        col=col+1;
        if m1(ii,k)>eps & m2(ii,k)>eps
            b(col,1)=log(m1(ii,k)/m2(ii,k));
            A(col,(row+1):(row+k-1)) = pixelsize; A(col,(row+k)) =0; A(col,(row+k+1):↙
(row+N)) = -pixelsize; % System matrix coefficient +/- pixelsize depends on position↙
relative to active pixel
        end
    end
    col=col+1;
    % Special case for column N
    if m1(ii,N)>eps & m2(ii,N)>eps
        b(col,1)=log(m1(ii,N)/m2(ii,N));
        A(col,(row+1):(row+N-1)) = pixelsize; A(col,(row+N)) = 0;
    end
    if (rem(ii,10) == 0)
        disp(ii)
    end
end
mus=-lsqr(A,b,0.001,100); mus=reshape(mus,N,N); % Atten coeffs recovered from inverse↙
solution
rotated_mus = flipud(rot90(mus));              % Rotate image to match ground truth↙
orientation

clear b
%%%%%% POISSON NOISE ADDED
col=0; A=zeros(1,N*N);
for ii =1:N
    row=N*(ii-1);
    col=col+1;
    if m1_poiss(ii,1)>eps & m2_poiss(ii,1)>eps
        b(col,1)=log(m1_poiss(ii,1)/m2_poiss(ii,1));
        A(col,row+1) = 0; A(col,(row+2):(row+N)) = -pixelsize;
    end
    for k=2:N-1
        col=col+1;
        if m1_poiss(ii,k)>eps & m2_poiss(ii,k)>eps
            b(col,1)=log(m1_poiss(ii,k)/m2_poiss(ii,k));
            A(col,(row+1):(row+k-1)) = pixelsize; A(col,(row+k)) =0; A(col,(row+k+1):↙
(row+N)) = -pixelsize;
        end
```

```
    end
    col=col+1;
    if m1_poiss(ii,N)>eps & m2_poiss(ii,N)>eps
        b(col,1)=log(m1_poiss(ii,N)/m2_poiss(ii,N));
        A(col,(row+1):(row+N-1)) = pixelsize; A(col,(row+N)) = 0;
    end
end
mus_poiss=-lsqr(A,b,0.001,100); mus_poiss=reshape(mus_poiss,N,N);
rotated_mus_poiss = flipud(rot90(mus_poiss));

%% Recover radiotracer concentration images

%%%%%% Pure m1 and m2 measurements
flux = zeros(N);fluxm1 = zeros(N);fluxm2 = zeros(N);concen = zeros(N);
for ii = 1:N
    for k = 2:N-1
        if m1(ii,k)>eps & m2(ii,k)>eps
            fluxm1(ii,k) = m1(ii,k)*exp(sum(rotated_mus(ii,1:k-1))*pixelsize); % perform↙
reverse Beer-Lambert law to recover intensity at each pixel
            fluxm2(ii,k) = m2(ii,k)*exp(sum(rotated_mus(ii,k+1:N))*pixelsize);
            flux(ii,k) = mean([fluxm1(ii,k) fluxm2(ii,k)]);   % Average both estimates
            concen(ii,k) = (flux(ii,k)*rotated_mus(ii,k))/(exp(-pixelsize*rotated_mus(ii,↙
k))*(exp(pixelsize*rotated_mus(ii,k))-1));
        end
    end
end

%%%%% Poisson Noise measurements
flux_poiss = zeros(N);fluxm1_poiss = zeros(N);fluxm2_poiss = zeros(N);concen_poiss =↙
zeros(N);
for ii = 1:N
    for k = 2:N-1
        if m1_poiss(ii,k)>eps & m2_poiss(ii,k)>eps
            fluxm1_poiss(ii,k) = m1_poiss(ii,k)*exp(sum(rotated_mus_poiss(ii,1:k-1))↙
*pixelsize);  % perform reverse Beer-Lambert law to recover concentration at each pixel
            fluxm2_poiss(ii,k) = m2_poiss(ii,k)*exp(sum(rotated_mus_poiss(ii,k+1:N))↙
*pixelsize);
            flux_poiss(ii,k) = mean([fluxm1_poiss(ii,k) fluxm2_poiss(ii,k)]);   % Average↙
both estimates
            concen_poiss(ii,k) = (flux_poiss(ii,k)*rotated_mus_poiss(ii,k))/(exp(-↙
pixelsize*rotated_mus_poiss(ii,k))*(exp(pixelsize*rotated_mus_poiss(ii,k))-1));
        end
    end
end
concen_poiss_scaled = concen_poiss./scalefactor;    % Divide out scale factor to recover↙
concentration values on true scale
```